Beam Shaping for Uniform and Energy-efficient Surface Structuring of Metals with Ultrashort Laser Pulses in the mJ Range

Daniel Holder[*1,2], Simon Hensel[1], Alexander Peter[1], Rudolf Weber[1], and Thomas Graf[1]

[1]*Institut für Strahlwerkzeuge (IFSW), University of Stuttgart, Pfaffenwaldring 43, 70569 Stuttgart, Germany*
[2]*ARENA2036 Research Campus, Pfaffenwaldring 19, 70569 Stuttgart, Germany*
[*]*Corresponding author's e-mail: daniel.holder@ifsw.uni-stuttgart.de*

Scaling the average power of ultrafast lasers into the kW range for high-throughput surface structuring and micromachining by the pulse energy requires an adapted processing strategy in order to minimize surface defects due to high fluences and maintain a high surface quality. One promising approach to distribute the pulse energy uniformly on the sample surface is spatial beam shaping using a spatial light modulator. The local phase was modulated by computer-generated holograms for the generation of uniform intensity distributions in the focal plane. The corresponding intensity distributions resulting from the different holograms were monitored with an on-axis camera to ensure accurate beam shapes during surface structuring and micromachining of the two materials stainless steel and cemented tungsten carbide. Uniform surface structures and flexible, dimensionally accurate cavities were machined with a shaped ultrafast laser beam and high pulse energies up to over 1 mJ on the sample surface. Various beam shapes with a cross-sectional area up to 0.42 mm² were generated on the sample surface for energy-efficient micromachining and homogenous surface structuring. The capability of high-energy pulse beam shaping was demonstrated by the fabrication of a large-area checkerboard pattern with small transition zones <10 µm between unprocessed and structured areas.
DOI: 10.2961/jlmn.2022.01.2006
Keywords: beam shaping, ultrashort laser pulses, spatial light modulator, computer-generated hologram, surface structuring, micromachining, stainless steel, cemented tungsten carbide

1. Introduction

Ultrafast lasers are an excellent tool for functionalization of material surfaces [1] and for micromachining of complex geometries with sizes and depths ranging from a few micrometers [2] up to several hundred micrometers [3]. Even demanding requirements such as the automated and local removal of exceeding material and smoothing of rough surfaces can be realized with this technology [3], [4]. Surface functionalization can be achieved by the generation of ripple-shaped laser-induced periodic surface structures (LIPSS) on the surface, that allow to locally modify the wettability, friction or optical properties [1], [5]. Such ripples are also generated during micromachining of deeper geometries and are often an indicator for low roughness and therefore high surface quality after the micromachining process [6], [7].

High throughput is required for the economical application of these processes in an industrial environment. In surface functionalization and micromachining, the throughput is defined by the structuring rate (structured area per time) and by the ablation rate (removed volume per time), respectively. In the past, a limiting factor was the low average power of the beam sources, which often prevented applicability for large-area or high-volume manufacturing. Recently, this situation has changed with the demonstrations of ultrafast lasers that exceed average powers of kW [7] even with excellent beam quality [8]. Various challenges and process limitations arise when processing with high average laser powers [9], [10], which require advanced system technology and process strategies to achieve high throughput while maintaining high surface quality. For the cases of surface structuring and micromachining at high pulse energies, a major challenge is maintaining a low fluence, which is only a few times over the material-specific ablation threshold in order to maintain a fine ripple structure [1] and high energy efficiency in micromachining [2]. Using pulse bursts and beam, high throughput micromachining with 1010 W average power and over 2 mJ pulse energy was demonstrated in [6] and [7] for silicon and different metals with ablation rates up to 230 mm³/min. Another promising approach using beam splitting was demonstrated in [11] with 200 W average laser power and 2 mJ pulse energy for high throughput surface structuring with structuring rates up to 1910 cm²/min.

Since standard ultrafast lasers have a Gaussian intensity distribution, this is also usually the intensity distribution which is used for processing. However, processing with a uniform intensity distribution, i.e. "top-hat", offers several advantages compared to a Gaussian intensity distribution: A higher maximum energy-efficiency at a lower optimum fluence is achieved in micromachining with a uniform intensity distribution [2], [12]. Besides, it allows micromachining of rectangular grooves without recast on the rims [13]. In surface structuring, the steeper intensity edges of a top-hat beam can be used to achieve smaller transition zones between unprocessed and structured areas, which allows for higher selectivity in ablation of thin films [13] and higher contrast in surface functionalization. Furthermore, a uniform

intensity distribution enables uniform surface structures inside the irradiated area [5] with higher structuring rate [14].

The Gaussian intensity distribution of the laser beam can be converted into a uniform intensity distribution by beam shaping. Several technical approaches for flexible beam shaping in microprocessing have been developed in the past few years. Recently, acousto-optical deflectors (AOD) have gained attention for beam shaping [15] due to the fast switching capabilities up to few hundreds of kHz [16]. The AOD can also be combined with a Galvanometer-scanner [17] or a diffractive optical element (DOE) for high-speed temporal and spatial beam-shaping [16]. Spatial light modulators (SLM) with computer-generated holograms (CGH) are a more common approach and can be used for the generation of arbitrary beam shapes with shape switching capabilities up to few tens of Hz [18], [19]. The SLM can also be combined with a Galvanometer-scanner [20] for beam shaping and scanning or combined with another SLM for beam shaping and beam splitting [21].

In this paper, beam shaping of ultrashort laser pulses with high pulse energies up to 1.27 mJ is demonstrated for uniform surface structuring of ripples with small transition zones and energy-efficient micromachining of large areas on metal samples. The potential of beam shaping for achieving a high surface quality even with high energy ultrafast lasers is shown in the following.

2. Methods and materials

2.1 Experimental setup for flexible beam shaping

The ultrafast laser system (*Spitfire ACE*, *Spectra Physics*) used for the experiments emitted pulses with a circular Gaussian intensity distribution centered at the wavelength $\lambda = 800$ nm, with a spectral bandwidth of 30 nm (FWHM, Gaussian fit) and with an adjustable pulse duration τ between 0.1 ps and 6.0 ps (FWHM, Gaussian fit). The maximum pulse energy E_P of 6 mJ at the pulse repetition rate of 1 kHz corresponds to a maximum average output power of 6 W. The laser beam had a beam quality factor of $M^2 < 1.3$ and was linearly polarized. Flexible beam shaping was performed using an SLM. The beam path with the 6f-optical setup between the SLM and the sample is shown in Fig. 1.

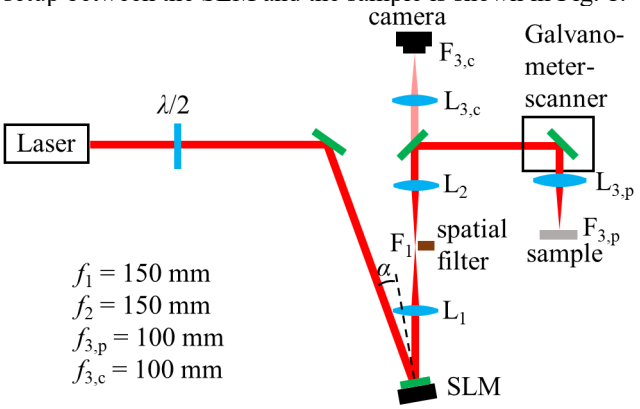

Fig. 1 Experimental setup used for laser surface structuring with flexible beam shapes.

A $\lambda/2$-waveplate was used to adjust the direction of polarization to a horizontal orientation. The experimental setup was designed to have an angle of incidence on the SLM of $\alpha < 5°$ in order to maximize the diffraction efficiency of the SLM. The beam diameter ($1/e^2$) on the SLM was measured to 10.0 mm using the knife-edge technique. The LCOS-SLM (*X13139*, *Hamamatsu*) had a fill factor of 96% and a resolution of 1272 x 1024 pixels with a pixel pitch of 12.5 µm, which corresponds to an effective field size of 16.0 mm x 12.8 mm. After modulation and reflection by the SLM, the beam was focused by the lens L_1 with a focal length of $f_1 = 150$ mm. A spatial filter was mounted in the focal plane F_1 in order to block the propagation of the 0th order and diffraction orders higher than the 1st diffraction order. The beam was collimated by the lens L_2 with $f_2 = 150$ mm and deflected into the Galvanometer-scanner (*intelliSCAN III 14*, *Scanlab*). The F-Θ lens $L_{3,p}$ with $f_{3,p} = 100$ mm focused the beam onto the sample, which was located in the focal plane $F_{3,p}$ of the F-Θ lens. The laser power and accordingly the pulse energy E_P used for processing was measured below the F-Θ lens $L_{3,p}$ to take power losses from optical elements and varying diffraction efficiency into account. A small portion of the average laser power was transmitted through the mirror which was located before the Galvanometer-scanner. The transmitted laser beam was focused by the lens $L_{3,c}$ with $f_{3,c} = 100$ mm onto a camera located in the focal plane $F_{3,c}$. The CMOS-camera (*µEye*, *IDS imaging*) with a pixel pitch of 5.2 µm was used to monitor the intensity distribution of the shaped laser beam. The dimensions of the beam shape monitored by the camera correspond to the dimensions of the beam shape used for material processing, as both lenses, $L_{3,p}$ and $L_{3,c}$ have an equal focal length $f_{3,p} = f_{3,c} = 100$ mm.

2.2 Analytical calculation of the holograms

Beam shaping was performed using different computer-generated holograms displayed on the SLM that modify the phase distribution of the beam. The fast analytical calculation of the holograms for the SLM according to [22] was used to create rectangles, squares and circles with uniform intensity distribution. The two dimensional phase function $\varphi(x,y)$ is calculated by

$$\varphi(x,y) = \beta_x \cdot \gamma_x(x) + \beta_y \cdot \gamma_x(y), \tag{1}$$

where the parameter

$$\beta = \frac{\sqrt{2\cdot\pi}\cdot r_{SLM}\cdot w_{3,p}}{f_{3,p}\cdot\lambda}, \tag{2}$$

and where r_{SLM} is the beam radius on the SLM, $w_{3,p}$ denotes the width of the desired beam shape in the focal plane $F_{3,p}$ of the lens with $f_{3,p}$ and corresponds to the edge length l_x or l_y (depending on the summand in Eq. (1)) of a rectangular or square beam shape or the diameter l_d of a circular beam shape. The one-dimensional solution of γ for rectangular or squared shapes is

$$\gamma(\xi) = \frac{\sqrt{\pi}\cdot\xi}{2}\cdot\mathrm{erf}(\xi) + \frac{1}{2}\cdot\exp\left(-\xi^2\right) - \frac{1}{2}, \tag{3}$$

where $\xi = \frac{\sqrt{2}\cdot x}{r_{SLM}}$ or $\xi = \frac{\sqrt{2}\cdot y}{r_{SLM}}$, depending on the dimension to be calculated. The solution of γ for a circular beam shape is given by

$$\gamma(\xi) = \frac{\sqrt{\pi}}{2}\cdot\int_0^{\xi}\sqrt{1-\exp\left(-\rho^2\right)}\,d\rho, \tag{4}$$

where $\xi = \frac{\sqrt{2} \cdot r}{r_{SLM}}$ and r denotes the radial distance from the optical axis. In order to separate the shaped top hat beam from the 0th order spatially, a blazed grating was added to the hologram, which allowed to block the 0th order in the F_1 plane without disturbing the shaped top hat beam.

2.3 Evaluation of the beam shaping quality

The camera images taken of the incident beam in the position $F_{3,c}$ (cf. Fig. 1) were used to measure the uniformity and edge steepness of the shaped intensity distribution. The uniformity of the beam directly influences the uniformity of surface structures and flatness of the micromachined surface. The beam uniformity

$$U_b = \frac{\sigma_b}{\mu_b} \quad (5)$$

was used to characterize the generated top hat beam, where σ_b is the standard deviation and μ_b is the mean intensity value of the evaluated area. $U_b = 0$ indicates a completely speckle-free and perfectly uniform intensity distribution. As an example, the evaluated area of a squared shaped beam with a desired edge length $l_x = l_y = 500$ µm as recorded by the camera is marked with a red dotted line in Fig. 2, where the beam uniformity was measured to $U_b = 0.08$. In the following diagrams, a measurement uncertainty of ±0.01 was taken into account by corresponding error bars.

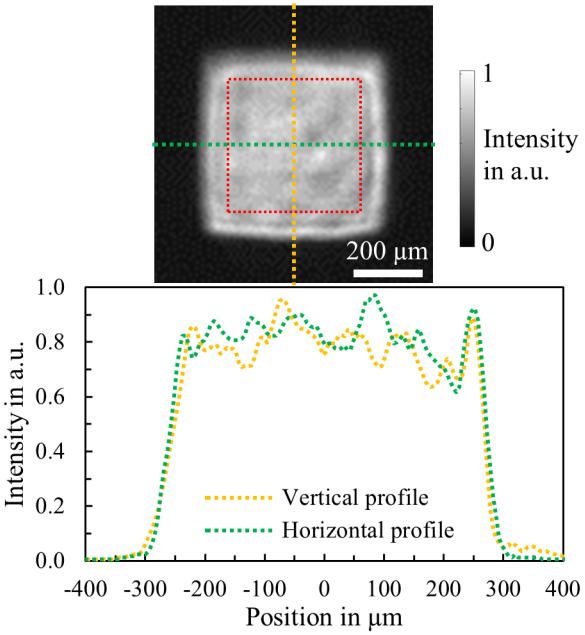

Fig. 2 Image of the squared beam shape generated by a hologram on the SLM as measured with the camera in the focal plane $F_{3,c}$ (top). The beam uniformity U_b was measured within the red squared area of the intensity distribution to $U_b = 0.08$. The yellow and green dotted lines correspond to the vertical and horizontal cross sections of the intensity distribution, respectively (bottom).

In material processing, the edge steepness of the shaped beam determines the extent of the transition zone between homogeneously structured areas due to the uniform intensity in the center area of the top hat and surrounding non-structured areas. The edge steepness

$$S_b = \frac{A_{10\%} - A_{90\%}}{A_{10\%}} \quad (6)$$

was used to characterize the generated top hat beam, where $A_{10\%}$ and $A_{90\%}$ are areas with intensity values above 10% and 90%, respectively, of the average intensity measured in the center area of the top hat. As can be seen from the profiles of the recorded top hat beam in Fig. 2 (yellow and green dotted lines), steep edges with a high contrast between the intensity plateau and surrounding area were achieved. The steepness of the vertical edges was measured to $S_b = 0.16 \pm 0.05$ and the steepness of the horizontal edges was measured $S_b = 0.13 \pm 0.05$.

2.4 Materials and evaluation of structured surfaces

Two different materials were used for the experiments: One sample was made from cemented tungsten carbide (TC), whereas tungsten carbide (90 wt%) with a grain size of 0.5 µm was bound in a Co-matrix (10 wt%). The other sample was made from stainless steel (SS) type AISI 304. Both of the samples were mechanically polished before surface structuring and micromachining. The surface structures resulting from structuring with the shaped beam as well as the extent of the transition zone between structured and non-structured areas were investigated using scanning electron microscopy (SEM, *Jeol*, *JSM-6490LV*). The micromachining process was characterized by the energy-specific volume ΔV_E, which was calculated by

$$\Delta V_E = \frac{\Delta V}{N \cdot E_P} \quad (7)$$

where ΔV is the removed material volume with N pulses of the pulse energy E_P. The removed material volume was measured with a laser scanning microscope (LSM, *VK-9700*, *Keyence*). In the following diagrams, the error bars represent an estimated measurement uncertainty of ±10%. The measured energy-specific volume was compared with the model presented in [2], which was modified for multiple pulses N, where the removed material volume can be calculated with

$$\Delta V = A_b \cdot N \cdot \delta_{eff} \cdot \ln\left(\frac{\phi}{\phi_{th}}\right) \quad (8)$$

where A_b denotes the cross-sectional area of the laser beam, δ_{eff} is the effective penetration depth, ϕ is the fluence given by $\phi = \frac{E_P}{A_b}$ and ϕ_{th} denotes the material-specific threshold fluence. The cross-sectional area is given by $A_b = l_x \cdot l_y$ for a rectangular or squared beam shape and by $A_b = \frac{\pi}{4} \cdot l_d^2$ for a circular beam shape.

3. Process limits for energy-efficient micromachining with flexible beam shapes and ultrashort laser pulses at high pulse energies

The energy-specific volume was measured for micromachining of tungsten carbide (TC) and stainless steel (SS) with a squared top hat beam with edge lengths $l_x = l_y = 200$ µm and different fluences ϕ and pulse durations τ. The cavities were micromachined with $N = 1000$ (TC) or $N = 300$ (SS) in order to receive a removed volume ΔV that

could be reliably measured with the LSM even at low fluences close to the ablation threshold ϕ_{th}. The energy-specific volumes are plotted in Fig. 3. Violet diamonds represent the results for TC and $\tau = 6.0$ ps, light blue diamonds represent the results for SS and $\tau = 6.0$ ps, and dark blue triangles represent the results for SS and $\tau = 0.5$ ps.

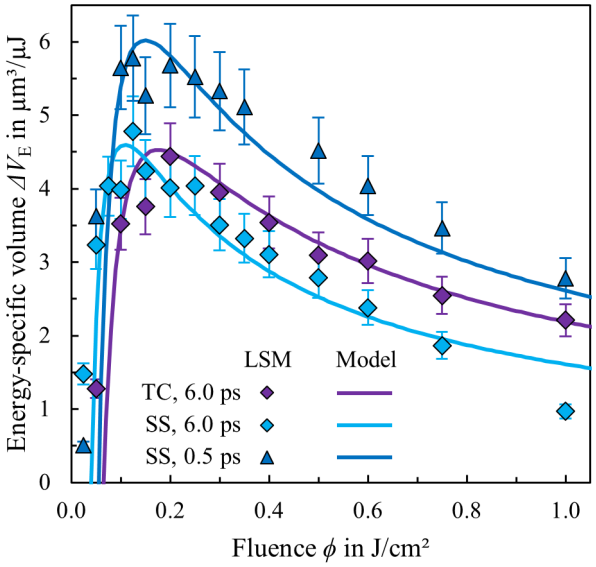

Fig. 3 Energy-specific volume ΔV_E as a function of the fluence ϕ for different materials (TC, SS) and pulse durations τ (6.0 ps, 0.5 ps) as measured by LSM and as calculated using the model in Eq. (7) and Eq. (8) and fitting the values δ_{eff} and ϕ_{th}.

The measured values show a well-pronounced maximum of ΔV_E in the range of $0.1 \le \phi \le 0.3$ J/cm². For $\phi > 0.3$ J/cm² the measured ΔV_E decreases, which is in good agreement with observations made in [20], [23]. The maximum value of ΔV_E is in the same range for TC and SS for micromachining with $\tau = 6.0$ ps, however the position of the maximum value is shifted to higher ϕ and a lower decrease of ΔV_E with increasing ϕ was measured for TC. A 35% higher maximum value for ΔV_E was measured for SS for micromachining with the shorter pulse duration $\tau = 0.5$ ps. The corresponding model curves from Eq. (7) and Eq. (8) are shown in Fig. 3 with continuous lines in the respective colors. The parameters δ_{eff} and ϕ_{th} were used for fitting the model curves to the measured values. A good fit was achieved for TC and $\tau = 6.0$ ps with $\delta_{eff} = 8$ nm and $\phi_{th} = 0.065$ J/cm², for SS and $\tau = 6.0$ ps with $\delta_{eff} = 5$ nm and $\phi_{th} = 0.040$ J/cm², and for SS and $\tau = 0.5$ ps with $\delta_{eff} = 9$ nm and $\phi_{th} = 0.055$ J/cm². The determined values for stainless steel are close to the values of $\delta_{eff} \approx 9$ nm and $\phi_{th} \approx 0.150$ J/cm² experimentally determined in [23], whereas the differences can result from a difference in the quality of the beam shape or the significantly increased edge length in this work. The determined values for the parameters δ_{eff} and ϕ_{th} in combination with the model from Eq. (7) and Eq. (8) provide a useful tool for the calculation of suitable beam cross-sectional areas and prediction of the ablated volume as a function of laser parameters and material properties.

Although micromachining with the shorter pulse duration is beneficial from an energy-efficient perspective, new challenges can arise for high-energy laser pulses with regard to beam uniformity. The measured beam uniformity U_b and camera images of the corresponding squared intensity distribution with $l_x = l_y = 200$ µm as a function of E_P for $\tau = 0.5$ ps (red triangles) and $\tau = 6.0$ ps (dark red diamonds) are shown in Fig. 4.

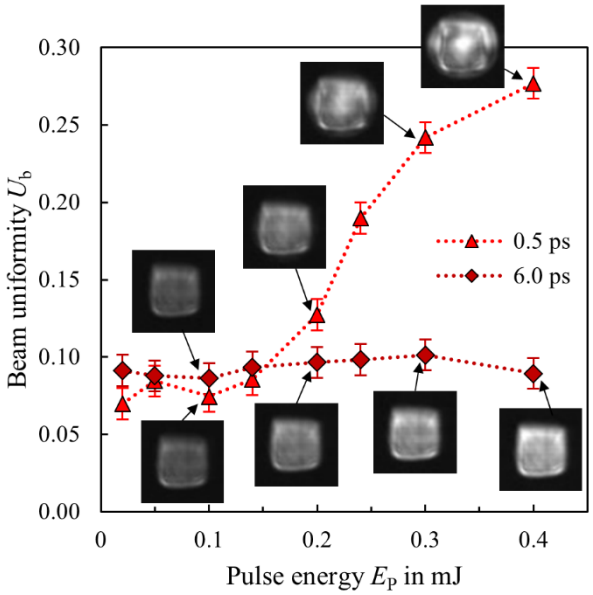

Fig. 4 Beam uniformity U_b of the squared top hat intensity distribution ($l_x = l_y = 200$ µm) measured from camera images with constant exposure time as a function of the pulse energy E_P for two different pulse durations, 0.5 ps and 6.0 ps.

The exposure time of the camera was fixed, which resulted in brighter camera images with increased pulse energy. For $\tau = 6.0$ ps, a uniform intensity distribution with $U_b < 0.1$ was observed independent of the pulse energy. For $\tau = 0.5$ ps and up to a pulse energy $E_P \le 0.14$ mJ, uniform intensity distributions with $U_b < 0.1$ were also observed. However, for pulse energies $E_P \ge 0.20$ mJ, U_b increased up to $U_b = 0.28$, indicating a decrease of the beam uniformity. This is visualized by the corresponding camera images shown in Fig. 4, as the shape of the beam became more distorted and the intensity in the center of the beam significantly increased with increasing pulse energy. The measured value of U_b is artificially reduced for $E_P = 0.4$ mJ due to the overexposure in the center of the image. The beam uniformity decreased at $\tau = 0.5$ ps and for $E_P > 0.14$ mJ due to a distortion of the phase distribution caused by the increased intensity of about one order of magnitude compared to $\tau = 6.0$ ps at similar pulse energy. The high intensity caused an air breakdown in the focal plane F_1 (cf. Fig. 1) between the lenses L_1 and L_2, which in turn distorted the phase of the propagating beam and resulted in a decrease of the uniformity of the shaped beam. With the setup used here, the pulse energy must be limited to $E_P = 0.14$ mJ (measured on the workpiece) at $\tau = 0.5$ ps to maintain high beam uniformity, which, assuming an identical maximum intensity in F_1 where the phase is not distorted by air breakdown, allows one to estimate the pulse energy limit for $\tau = 6.0$ ps to be about $E_P = 1.40$ mJ (on the workpiece in $F_{3,p}$).

Due to the limited usable pulse energy at $\tau = 0.5$ ps with regard to beam uniformity, further investigations in this work were only performed with $\tau = 6.0$ ps. The resulting surface structures from micromachining of TC and SS with $\tau = 6.0$ ps, $N = 1000$ and different ϕ as measured by SEM are shown in Fig. 5.

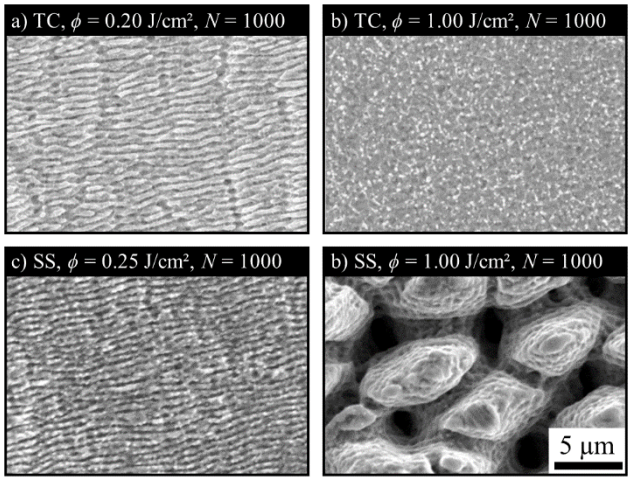

Fig. 5 SEM images of surface structures generated on tungsten carbide (TC) and stainless steel (SS) after irradiation with N = 1000 and τ = 6.0 ps and with different fluences ϕ.

Ripples with a period of 0.7±0.1 µm were observed for TC and SS for low fluences ϕ about 3 to 6 times the threshold fluence ϕ_{th} (Fig. 5 a) and c)). The period of the ripples is correlated with the wavelength of laser beam of λ = 800 nm [1]. For high fluences ϕ about 15 to 20 times the threshold fluence ϕ_{th}, completely different structures can be observed on the two materials. A surface only partly covered by ripples and with adherent nanoparticles was observed on TC (Fig. 5 b). A very rough surface covered with spikes of up to 10 µm in diameter and height was found on SS (Fig. 5 d).

With regard to process limits, the results emphasize the need to limit the local fluence to about 3 to 6 times the threshold fluence ϕ_{th} in order to achieve rather smooth surfaces covered uniformly only by ripple structures. For micromachining applications, this behavior coincides well with the range of fluence required for a high energy-specific volume ΔV_E, as shown in Fig. 3. Higher pulse energies can be used in a 6f-optical setup by using longer pulse durations, as the lower intensity in F_1 reduces phase distortions that can result in a distorted beam shape.

4. Influence of the beam shape on the uniformity and efficiency in micromachining

Within the process limits described in the previous section, the laser beam was shaped using different holograms in order to receive squared ($l_x = l_y$ = 600 µm), rectangular (l_x = 800 µm, l_y = 450 µm) and circular (l_d = 650 µm) beam shapes. The different intensity distributions as measured with the camera in the focal place $F_{3,c}$ are depicted in the top of Fig. 6. A uniform intensity distribution was achieved for the squared top hat and rectangular top hat. Only the circular top hat showed a local intensity increase on the bottom left, indicated by the brighter area, presumably caused by a slight misalignment of the experimental setup.

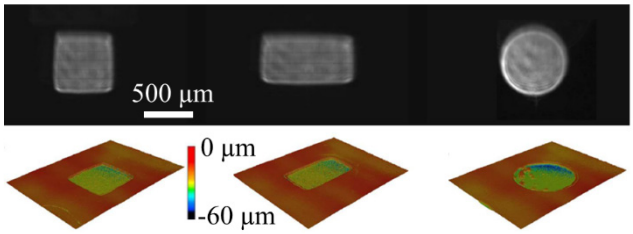

Fig. 6 Camera images of shaped beam intensity distributions generated by different holograms on the SLM measured in the focal plane $F_{3,c}$ (top) and corresponding LSM measurements of the generated cavities in the focal plane $F_{3,p}$ on stainless steel by micromachining with τ = 6 ps, ϕ = 0.25 J/cm² and N = 1000 (bottom).

The corresponding micromachining results are depicted in the bottom of Fig. 6. A uniformly ablated area was achieved with the squared and rectangular top hat due to the uniform intensity distribution. The local intensity increase of the circular beam shape on the bottom left area resulted in an increased local fluence, which caused the local formation of spikes in this area, indicated by the small red spikes.

The energy-specific volume ΔV_E of the different beam shapes - square, rectangle and circle - at similar beam cross-sectional areas $0.33 \leq A_b \leq 0.36$ mm² was measured for τ = 6 ps, ϕ = 0.26 J/cm² and N = 300 and is plotted in Fig. 7 by a blue square, a blue rectangle and a blue circle, respectively. It is worth noting that the pulse energy was measured for each shape and each beam cross-sectional area on the workpiece after $L_{3,p}$ in order to account for differences in losses, e.g. due to a different diffraction efficiency.

The values of ΔV_E for the different shapes at similar beam cross-sectional areas $0.33 \leq A_b \leq 0.36$ mm² were within the measurement error, indicating that the beam shape did not influence the energy-specific volume ΔV_E. However, a significant decrease of ΔV_E was measured with increasing beam cross-sectional area A_b, from ΔV_E = 4.0 µm³/µJ at A_b = 0.04 mm² to ΔV_E = 2.7 µm³/µJ at A_b = 0.36 mm², which corresponds to a reduction of about 33%. The decrease of ΔV_E appears to go into saturation. For $A_b > 0.36$ mm² no significant reduction of ΔV_E was observed. A similar behavior was measured for micromachining with gaussian-shaped beams [23], [24]. The uniformity of the beam was $U_b < 0.1$ regardless of the shape and cross-sectional area of the beam. An additional quality criterion such as the maximum deviation to the mean intensity value is required in order to quantitatively describe and identify a local intensity increase as found for the circular top hat.

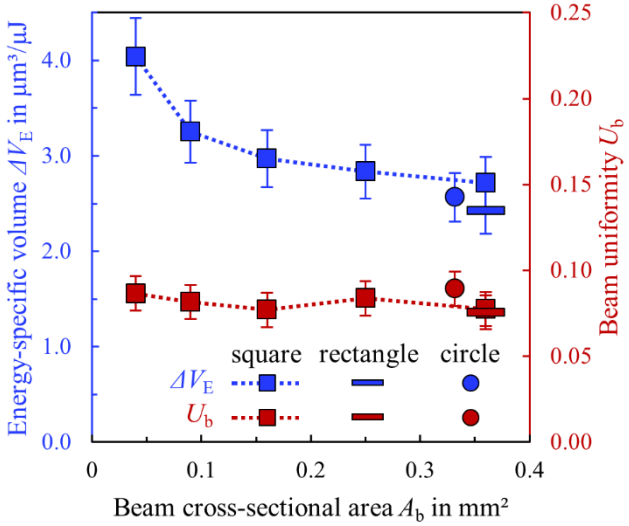

Fig. 7 Energy-specific volume ΔV_E and beam uniformity U_b as a function of the beam cross-sectional area A_b for different beam shapes with different edge lengths or radius. The removed volume was measured with an LSM for micromachining of SS with τ = 6 ps, ϕ = 0.26 J/cm² and N = 300. The beam uniformity was measured from camera images during micromachining. The dotted lines connecting the data points were drawn to guide the eye.

5. Large-area uniform surface structuring with ultrashort laser pulses in the mJ range

The combination of an SLM with a Galvanometer-scanner allows for large-area surface structuring with a shaped laser beam by rasterizing the beam over the sample surface. In the following, this is demonstrated for a squared sample of stainless steel with edge lengths of 25 x 25 mm². 740 squares with an edge length of $l_x = l_y = 650$ µm ($A_b = 0.42$ mm²) were structured with $N = 30$ in a checkerboard pattern, as shown in the camera image in the bottom left of Fig. 8.

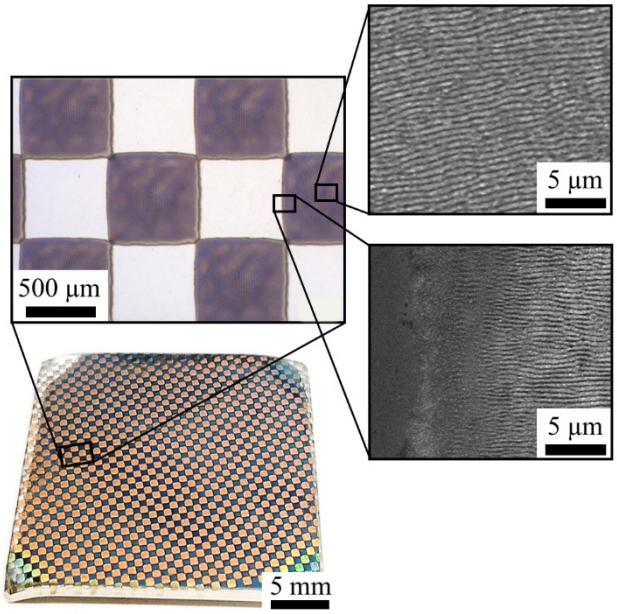

Fig. 8 Camera image of a large-area checkerboard pattern on a stainless steel sample from oblique view after structuring of 740 squares with an edge length of 650 µm each using $\tau = 6$ ps, $E_P = 1.27$ mJ, $\phi = 0.30$ J/cm² and $N = 30$ (bottom left). The colors on the structured sample are created by the diffraction effect caused by the periodic ripple structures (SEM image, top right). The magnifications from the optical microscope (top left) and SEM (bottom right), respectively, show the uniformity of the squares and the small extend of the transition zone between unprocessed and structured areas.

A pulse duration of $\tau = 6$ ps was used to avoid phase distortions in the focal plane F_1 at the high pulse energy of $E_P = 1.27$ mJ on the workpiece in $F_{3,p}$. Considering the diffraction efficiency of 69% and transmission of the optical setup of 65%, the pulse energy irradiated on the SLM was about $E_P = 2.88$ mJ. Even with this high pulse energy irradiated on the SLM, no degradation of the beam shaping quality or damage to the SLM was observed. The magnification (Fig. 8, top left) shows the accurate arrangement of the structured squares on the sample surface. The uniform intensity distribution of the beam caused a homogeneous formation of ripples all over the squared structure (Fig. 8, top right). The extent of the transition zone between unprocessed and uniformly structured areas is <10 µm (Fig. 8, bottom right), which corresponds to only 6% of the structured surface area of $A_b = 0.42$ mm² per pulse. It is worth noting that the transition zone is <10 µm, although the extent of the edge zone of the intensity profile in Fig. 2 is in the range of 30 µm to 50 µm. This difference can be explained by the ratio of local fluence to ablation threshold: At local fluences in the range of the threshold fluence at $\phi_{th} = 0.04$ J/cm², the generated ripple structures are low pronounced and therefore the transition zone appears smeared. This area corresponds to the very bottom of the edge zone. At fluences well above the threshold fluence, the ripple structures generated are strongly pronounced along the edge to the plateau at $\phi = 0.30$ J/cm². The small transition zone allows a high contrast of the functionality of the unprocessed area and the structured area, e.g. with regard to the wettability, friction or absorptivity. The results show that large-area and uniform surface structuring with flexible beam shapes can be achieved with ultrashort laser pulses even at high pulse energies in the mJ range. With the development of SLMs capable of handling high average powers up to over 200 W [25], the presented results here pave the way for high throughput surface structuring with uniform intensity distributions.

6. Conclusion

In summary, beam shaping of ultrashort laser pulses with high pulse energy was performed using computer-generated holograms on a spatial light modulator for uniform surface structuring and energy-efficient micromachining of large areas on metal samples.

Process limits have been determined that must be adhered to in order to achieve uniform intensity distribution and a high quality surface: The local fluence on the workpiece must be limited to 3 to 6 times the ablation threshold in order to achieve the maximum energy-specific volume and a surface covered by ripples. Although a 35% higher maximum energy-specific volume was achieved for micromachining stainless steel by using a pulse duration of 0.5 ps instead of 6 ps, the pulse duration can be a limiting factor with regard to exceeding a critical intensity threshold. If the intensity in the first focal plane of the 6f-optical setup - which is often used for spatial filtering of the 0th order and diffraction orders higher than the 1st order - exceeds a certain value, phase distortions can occur from an air breakdown in the focal plane which result in beam deformation and significant decrease in beam uniformity.

By staying within the process limits, different beam shapes such as square, rectangle and circle could be realized with high beam uniformity and were used to investigate the influence of the beam shape and beam size on the energy-specific volume. No significant influence of the beam shape was observed, but a significant decrease in energy-specific volume was measured with increasing the beam cross-sectional area, the cause of which needs to be investigated in future work.

Finally, squared-shaped laser pulses with an edge length of 650 µm and having a pulse duration of 6 ps and a pulse energy of more than 1 mJ were used to demonstrate large-area uniform surface structuring of fine ripples on stainless steel. The extent of the transition zone between unprocessed and uniformly structured areas is <10 µm, which corresponds to only 6% of the structured surface area of 0.42 mm² per pulse. The results shown here prove the high potential of beam shaping for achieving a high surface quality even with high-energy ultrafast lasers.

Funding

This work was supported by the Federal Ministry for Economic Affairs and Climate Action (BMWK) in the frame of

the project “BionicTools” (03EN4007G) and funded by the Deutsche Forschungsgemeinschaft (DFG, German Research Foundation) – INST 41/1031–1 FUGG.

References

[1] J. Bonse, S. Höhm, S.V. Kirner, A. Rosenfeld, and J. Krüger: IEEE J. Select. Topics Quantum Electron., 23, (2017) 9000615.
[2] B. Neuenschwander, G.F. Bucher, C. Nussbaum, B. Joss, M. Muralt, U.W. Hunziker, and P. Schuetz: Proc. SPIE, Vol. 7584, (2010) 75840R.
[3] D. Holder, M. Buser, A. Leis, R. Weber, and T. Graf: IOP Conf. Ser.: Mater. Sci. Eng., 1135, (2021) 12005.
[4] D. Holder, A. Leis, M. Buser, R. Weber, and T. Graf: Adv. Opt. Technol., 9, (2020) 101.
[5] A. Möhl, S. Kaldun, C. Kunz, F.A. Müller, U. Fuchs, and S. Gräf: J. Laser Appl., 31, (2019) 42019.
[6] D. Holder, R. Weber, C. Röcker, G. Kunz, D. Bruneel, M. Delaigue, T. Graf, and M. Abdou Ahmed: Opt. Lett., 46, (2021) 384.
[7] M. Abdou Ahmed, C. Roecker, A. Loescher, F. Bienert, D. Holder, R. Weber, V. Onuseit, and T. Graf: Adv. Opt. Technol., 10, (2021) 285.
[8] A. Loescher, F. Bienert, C. Röcker, T. Graf, M. Gorjan, J. aus der Au, and M. Abdou Ahmed: Opt. Continuum, 1, (2022) 747.
[9] R. Weber and T. Graf: Adv. Opt. Technol., 10, (2021) 239–245.
[10] D. Brinkmeier, D. Holder, A. Loescher, C. Röcker, D.J. Förster, V. Onuseit, R. Weber, M. Abdou Ahmed, and T. Graf: Appl. Phys. A, 128, (2022).
[11] P. Hauschwitz, J. Martan, R. Bičišťová, C. Beltrami, D. Moskal, A. Brodsky, N. Kaplan, J. Mužík, D. Štepánková, J. Brajer, D. Rostohar, J. Kopeček, L. Prokešová, M. Honner, V. Lang, M. Smrž, and T. Mocek: Sci. Rep., 11, (2021) 22944.
[12] K. Du: Proc. SPIE, Vol. 7202, (2009) 72020Q.
[13] G. Račiukaitis, E. Stankevičius, P. Gečys, M. Gedvilas, C. Bischoff, E. Jäger, U. Umhofer, and F. Völklein: J. Laser Micro Nanoeng., 6, (2011) 37.
[14] M. El-Khoury, B. Voisiat, T. Kunze, and A.F. Lasagni: Materials, 15, (2022) 591.
[15] T. Häfner, J. Strauß, C. Roider, J. Heberle, and M. Schmidt: Appl. Phys. A, 124, (2018) 111.
[16] J. Linden, S. Cohen, Y. Berg, I. Peled, Z. Kotler, and Z. Zalevsky: Opt. Express, 29, (2021) 31229.
[17] D. Franz, T. Häfner, T. Kunz, G.-L. Roth, S. Rung, C. Esen, and R. Hellmann: Appl. Phys. B, 128, (2022) 55.
[18] N. Sanner, N. Huot, E. Audouard, C. Larat, and J.-P. Huignard: Opt. Lasers Eng., 45, (2007) 737.
[19] D.G. Grossmann, D. Flamm, J. Hellstern, M. Sailer, and M. Kumkar: Proc. SPIE, Vol. 11267, (2020) 112670R.
[20] T. Häfner, J. Heberle, D. Holder, and M. Schmidt: J. Laser Appl., 29, (2017) 22205.
[21] J. Li, Y. Tang, Z. Kuang, J. Schille, U. Loeschner, W. Perrie, D. Liu, G. Dearden, and S. Edwardson: Opt. Lasers Eng., 112, (2019) 59.
[22] F.M. Dickey, L.S. Weichman, and R.N. Shagam: Proc. SPIE, Vol. 4065, (2000) 338.
[23] M. Chaja, T. Kramer, and B. Neuenschwander: Procedia CIRP, 74, (2018) 300.
[24] B. Lauer, B. Jaeggi, Y. Zhang, and B. Neuenschwander: Proc. ICALEO, 2015, (2015) 146.
[25] G. Zhu, D. Whitehead, W. Perrie, O.J. Allegre, V. Olle, Q. Li, Y. Tang, K. Dawson, Y. Jin, S.P. Edwardson, L. Li, and G. Dearden: J. Phys. D: Appl. Phys., 51, (2018) 95603.

(Received: May 16, 2022, Accepted: July 18, 2022)